Publication Year	2020
Acceptance in OA	2021-11-16T15:41:42Z
Title	Properties of the dense core population in Orion B as seen by the Herschel Gould Belt survey
Authors	Könyves, V., André, Ph., Arzoumanian, D., Schneider, N., Men'shchikov, A., Bontemps, S., Ladjelate, B., Didelon, P., PEZZUTO, Stefano, BENEDETTINI, Milena, Bracco, A., Di Francesco, J., Goodwin, S., Rygl, K. L. J., Shimajiri, Y., SPINOGLIO, Luigi Giuseppe Maria, Ward-Thompson, D., White, G. J.
Publisher's version (DOI)	10.1051/0004-6361/201834753
Handle	http://hdl.handle.net/20.500.12386/31091
Journal	ASTRONOMY & ASTROPHYSICS
Volume	635

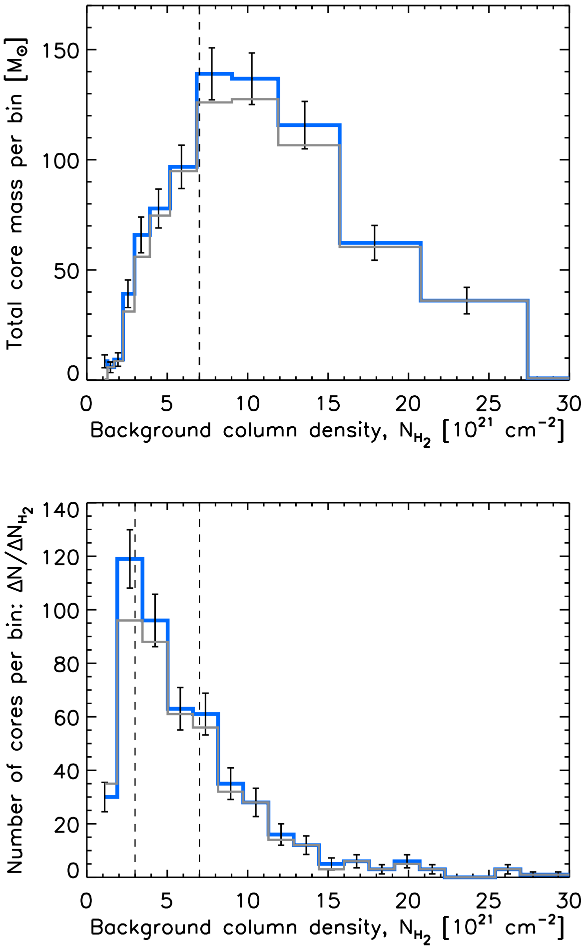

Fig. 17. *Top*: total mass in form of prestellar cores as function of ambient cloud column density in Orion B (blue histogram). *Bottom*: distribution of background column densities for the 490 *robust* prestellar cores (blue histogram). The vertical dashed lines mark $A_V^{bg} \sim 3$ and 7 mag. The overlaid gray histograms show the same distributions excluding the cores lying in the northern region L1622, which are at a more uncertain distance (see Sects. 1 and 3.5.2 for details).

gas filaments (Ostriker 1964; Inutsuka & Miyama 1997), and to a threshold volume density $n_{H_2}^{th} \sim 3 \times 10^4\,\mathrm{cm}^{-3}$. Alternatively, under the extreme assumption that the background cloud structure is completely isotropic, one can derive another conversion between column density and typical volume density (cf. Fig. A.1d of Bron et al. 2018), which leads to a significantly lower value of only $\sim 10^3\,\mathrm{cm}^{-3}$ for the threshold volume density. Obviously, only an order-of-magnitude estimate of the threshold volume density can be derived. Because the *Herschel* data indicate that the local background around each core is highly anisotropic (e.g., filamentary), we nevertheless tend to favor our higher estimate of the threshold volume density (i.e., $\sim 3 \times 10^4\,\mathrm{cm}^{-3}$).

4.6. Lifetime of prestellar cores in Orion B

As our *Herschel* survey provides an essentially complete census of prestellar cores in the Orion B clouds, the core statistics can be used to set constraints on the typical lifetime of prestellar cores and the timescale of the core formation process. We may derive a rough lifetime by comparing the number of prestellar cores found here with *Herschel* to the number of Class II YSOs detected in the mid-IR by *Spitzer* in the same region. The same approach was first used by Beichman et al. (1986) based on IRAS data. Our findings will hold, assuming that (1) all prestellar cores will evolve into YSOs in the future, and (2) star formation proceeds at a roughly constant rate, at least when averaged over the entire Orion B cloud complex.

The three HGBS tiles imaged with *Herschel* around NGC 2023 and 2024, NGC 2068 and 2071, and L1622 (see, e.g., Fig. 2) were also observed by IRAC as part of the *Spitzer* Orion survey (Megeath et al. 2012) and thus provide a common field where *Herschel* and *Spitzer* source counts can be directly compared. The various numbers of dense cores and YSOs identified by the two surveys in this common field are as follows:

- *Herschel* starless cores: 1032; above the mass completeness limit of 0.4 $M_\odot$: 338
- *Herschel candidate* prestellar cores: 538; above 0.4 $M_\odot$: 333
- *Herschel robust* prestellar cores: 361; above 0.4 $M_\odot$: 312
- *Spitzer* Class II YSOs: 312; corrected for incompleteness: 427
- *Spitzer* entire sample of Class 0/I–flat spectrum–Class II YSOs: 428; corrected for incompleteness: 586.

For our lifetime estimates, we used the numbers of *Spitzer* sources corrected for incompleteness with the help of *Chandra* data and other techniques as described in detail in Megeath et al. (2016). In practice, the corrected numbers of *Spitzer* sources were derived by multiplying the uncorrected number counts by a factor of 1.37, based on Table 1 of Megeath et al. (2016).

If we adopt a reference lifetime of 2 Myr for Class II YSOs (Evans et al. 2009), the comparison between *Herschel* and *Spitzer* source counts leads to lifetimes ranging from $2 \times 312/586 \approx 1.1$ Myr to $2 \times 538/427 \approx 2.5$ Myr for the prestellar core phase, depending on whether we consider only *robust* prestellar cores above our mass completeness limit of 0.4 $M_\odot$ or all *candidate* prestellar cores, and all *Spitzer* YSOs up to Class II or only YSOs nominally classified as Class IIs. Our best estimate of the prestellar core lifetime in Orion B is thus $t_{pre}^{OrionB} = 1.7_{-0.6}^{+0.8}$ Myr, derived from the ratio 361/427 of the total number of *Herschel* prestellar cores to the number of *Spitzer* Class II YSOs corrected for incompleteness. This is slightly longer than, but consistent within errors with, the prestellar lifetime estimate derived by Könyves et al. (2015) in the Aquila cloud, $t_{pre}^{Aquila} = 1.2 \pm 0.3$ Myr.

As a result of non-uniform incompleteness effects between the *Spitzer* and the *Herschel* sample, the uncertainties in these lifetimes are admittedly rather large (at least a factor of ~2). Additional sources of errors possibly affecting the above lifetime estimate are: (1) Megeath et al. (2012) used infrared spectral index values uncorrected for extinction (in Aquila, the compared *Spitzer* sources had been dereddened), (2) the classification of cores and YSOs is somewhat uncertain, and (3) the two initial assumptions mentioned above (i.e., prestellar nature of the cores and steady state) may not entirely hold.

5. Summary and conclusions

Using SPIRE and PACS parallel-mode data from the *Herschel* Gould Belt survey, we obtained an extensive census of dense cores in the Orion B star-forming region. We analyzed both the physical properties of the cores and the connection with interstellar filaments. Our main results and conclusions can be summarized as follows:

1. As in other HGBS clouds, the high-resolution (~18″ or ~ 0.03 pc) *Herschel* column density map of Orion B shows

a highly filamentary distribution of matter and the column density PDF features a prominent power-law tail above $A_{\rm V} \sim 3$ mag.
2. Based on multi-scale, multi-wavelength core extraction with the `getsources` algorithm we identified 1768 starless dense cores, 804 *candidate* prestellar cores, 490 *robust* prestellar cores, and 76 protostellar cores in the ∼19 deg^2 field that was imaged with both SPIRE and PACS at five wavelengths between 70 μm and 500 μm. The ∼80% mass completeness level for *candidate* prestellar cores was estimated to be at an observed core mass of $\sim 0.4\,M_\odot$. The *candidate* prestellar cores have an estimated median mass $\sim 0.5\,M_\odot$, a median deconvolved FWHM diameter ∼0.03 pc, a median average column density $\sim 4 \times 10^{21}$ cm^{-2}, and a median average volume density $\sim 3 \times 10^{4}$ cm^{-3}.
3. The identified dense cores are closely associated with filamentary structures. A very high fraction of prestellar cores (60–90%) were found within the 0.1 pc inner portion of the filaments extracted with both DisPerSE and `getfilaments`. Considering the deep raw sample of filaments extracted with DisPerSE, we find that almost all dense cores (>90%) lie within – stronger or fainter – elongated filamentary structures. Filaments may provide a more optimal environment for the growth of prestellar cores than spheroidal clumps.
4. The most massive prestellar cores in our sample (with masses between $M \sim 2\,M_\odot$ and $\sim 10\,M_\odot$) tend to be spatially segregated in the highest column density portions of the Orion B cloud, at equivalent visual extinctions $A_{\rm V}^{\rm bg} \gtrsim 15$–30. In particular, the distribution of median prestellar core mass as a function of background column density (Fig. 12) shows that both the median core mass and the dispersion in core masses increase roughly linearly with background column density. This suggests that the prestellar core mass function (CMF) may not be strictly universal but may depend on the local column density in the ambient cloud. This also suggests that intermediate-mass and high-mass protostars may form only (or at least preferentially) in the dense inner portions of molecular clouds, supporting the notion of primordial mass segregation in stellar protoclusters.
5. The global differential CMF derived for the whole sample of 804 *candidate* prestellar cores (or 490 *robust* prestellar cores) peaks at $\sim 0.5\,M_\odot$ (in $\Delta N/\Delta \log M$ format), which is just above the estimated 80% completeness limit of $\sim 0.4\,M_\odot$ in Orion B. The best power-law fit to the high-mass end of the prestellar CMF has a slope of -1.27 ± 0.24, compared to the Salpeter slope of -1.35 (Fig. 13).
6. Splitting the global sample of Orion B prestellar cores in a subsample of cores observed at high background column densities ($A_{\rm V}^{\rm bg} \geq 15$) and a subsample of cores observed at low and intermediate background column densities ($A_{\rm V}^{\rm bg} < 7$), we found that the CMF of the high-$A_{\rm V}$ subsample peaks at an order of magnitude higher mass ($\sim 3.8\,M_\odot$) than the lower $A_{\rm V}$ subsample ($\sim 0.4\,M_\odot$) (Fig. 14). This result, which cannot be explained by differential incompleteness effects, further illustrates the presence of significant mass segregation in the prestellar core population of the cloud.
7. The *Herschel* data in Orion B confirm the presence of a column density transition around $A_{\rm V}^{\rm bg} \sim 5-10$, for the formation of prestellar cores (Fig. 16). Coupled to the close connection observed between cores and filaments (point 3), this is consistent with the view that dense filamentary structures with line masses near or above the thermal value of the critical mass per unit length of isothermal cylinders provide the most favorable local environment for prestellar cores to grow within molecular clouds.
8. The typical lifetime of *Herschel* prestellar cores in Orion B was estimated to be $t_{\rm pre}^{\rm OrionB} = 1.7^{+0.8}_{-0.6}$ Myr, which is consistent within error bars with the prestellar core lifetime $t_{\rm pre}^{\rm Aquila} = 1.2 \pm 0.3$ Myr derived by Könyves et al. (2015) in the Aquila cloud.

Acknowledgements. SPIRE has been developed by a consortium of institutes led by Cardiff Univ. (UK) and including: Univ. Lethbridge (Canada); NAOC (China); CEA, LAM (France); IFSI, Univ. Padua (Italy); IAC (Spain); Stockholm Observatory (Sweden); Imperial College London, RAL, UCL-MSSL, UKATC, Univ. Sussex (UK); and Caltech, JPL, NHSC, Univ. Colorado (USA). This development has been supported by national funding agencies: CSA (Canada); NAOC (China); CEA, CNES, CNRS (France); ASI (Italy); MCINN (Spain); SNSB (Sweden); STFC, UKSA (UK); and NASA (USA). PACS has been developed by a consortium of institutes led by MPE (Germany) and including UVIE (Austria); KUL, CSL, IMEC (Belgium); CEA, OAMP (France); MPIA (Germany); IFSI, OAP/AOT, OAA/CAISMI, LENS, SISSA (Italy); IAC (Spain). This development has been supported by the funding agencies BMVIT (Austria), ESA-PRODEX (Belgium), CEA/CNES (France), DLR (Germany), ASI (Italy), and CICT/MCT (Spain). V.K. would like to thank Richard Allison, and Richard Parker for their help and discussions on mass segregation with the MST method. This work has received support from the European Research Council under the European Union's Seventh Framework Programme (ERC Advanced Grant Agreements no. 291294 – ORISTARS – and no. 267934 – MISTIC) and from the French National Research Agency (Grant no. ANR–11–BS56–0010 – STARFICH). D.A. acknowledges support by FCT/MCTES through national funds (PIDDAC) by the grant UID/FIS/04434/2019. N.S. and S.B. acknowledge support by the French ANR and the German DFG through the project GENESIS (ANR–16–CE92–0035–01/DFG1591/2–1). G.J.W. gratefully acknowledges support from The Leverhulme Trust. We also acknowledge support from the French national programs of CNRS/INSU on stellar and ISM physics (PNPS and PCMI). This research has made use of the SIMBAD database, operated at CDS, Strasbourg (France), and of the NASA/IPAC Extragalactic Database (NED), operated by the Jet Propulsion Laboratory, California Institute of Technology, under contract with the National Aeronautics and Space Administration.

References

Allison, R. J., Goodwin, S. P., Parker, R. J., et al. 2009, MNRAS, 395, 1449
Alves, J., Lombardi, M., & Lada, C. J. 2017, A&A, 606, L2
André, P., Belloche, A., Motte, F., & Peretto, N. 2007, A&A, 472, 519
André, P., Men'shchikov, A., Bontemps, S., et al. 2010, A&A, 518, L102
André, P., Di Francesco, J., Ward-Thompson, D., et al. 2014, in Protostars and Planets VI, eds. H. Beuther et al. (Tucson: University of Arizona Press), 27
André, P., Könyves, V., Arzoumanian, D., & Roy, A. 2017, Mem. Soc. Astron. It., 88, 521
André, P., Arzoumanian, D., Könyves, V., Shimajiri, Y., & Palmeirim, P. 2019, A&A, 629, L4
Arzoumanian, D., André, P., Didelon, P., et al. 2011, A&A, 529, L6
Arzoumanian, D., André, P., Peretto, N., & Könyves, V. 2013, A&A, 553, A119
Arzoumanian, D., André, P., Könyves, V., et al. 2019, A&A, 621, A42
Bally, J. 2008, Handbook of Star Forming Regions, ed. B. Reipurth (San Francisco: ASP), 459
Beichman, C. A., Myers, P. C., Emerson, J. P., et al. 1986, ApJ, 307, 337
Benedettini, M., Schisano, E., Pezzuto, S., et al. 2015, MNRAS, 453, 2036
Benedettini, M., Pezzuto, S., Schisano, E., et al. 2018, A&A, 619, A52
Bernard, J.-P., Paradis, D., Marshall, D. J., et al. 2010, A&A, 518, L88
Bohlin, R. C., Savage, B. D., & Drake, J. F. 1978, ApJ, 224, 132
Bontemps, S., André, P., Könyves, V., et al. 2010, A&A, 518, L85
Bouwman, J. 2001, PhD Thesis, University of Amsterdam, The Netherlands
Bouwman, J., de Koter, A., van den Ancker, M. E., & Waters, L. B. F. M. 2000, A&A, 360, 213
Bresnahan, D., Ward-Thompson, D., Kirk, J. M., et al. 2018, A&A, 615, A125
Bron, E., Daudon, C., Pety, J., et al. 2018, A&A, 610, A12
Casertano, S., & Hut, P. 1985, ApJ, 298, 80
Chabrier, G. 2005, Astrophys. Space Sci. Lib., 327, 41
Cox, N. L. J., Arzoumanian, D., André, P., et al. 2016, A&A, 590, A110
Dib, S., & Henning, T. 2019, A&A, 629, A135
Dunham, M. M., Crapsi, A., Evans, II, N. J., et al. 2008, ApJS, 179, 249
Elmegreen, B. G., & Falgarone, E. 1996, ApJ, 471, 816
Evans, II, N. J., Dunham, M. M., Jørgensen, J. K., et al. 2009, ApJS, 181, 321
Finkbeiner, D. P. 2003, ApJS, 146, 407

Gini, C. 1912, in Variabilità e mutabilità, Reprinted in Memorie di Metodologia Statistica (eds. E. Pizetti, T. Salvemini), Rome: Libreria Erendi Virgilio Veschi (Berlin: Springer), 1955

Griffin, M. J., Abergel, A., Abreu, A., et al. 2010, A&A, 518, L3+

Gutermuth, R. A., Megeath, S. T., Myers, P. C., et al. 2009, ApJS, 184, 18

Hatchell, J., Richer, J. S., Fuller, G. A., et al. 2005, A&A, 440, 151

Hennemann, M., Motte, F., Schneider, N., et al. 2012, A&A, 543, L3

Heyer, M., Krawczyk, C., Duval, J., & Jackson, J. M. 2009, ApJ, 699, 1092

Hildebrand, R. H. 1983, QJRAS, 24, 267

Inutsuka, S.-I., & Miyama, S. M. 1997, ApJ, 480, 681

Johnstone, D., Di Francesco, J., & Kirk, H. 2004, ApJ, 611, L45

Kirk, H., Di Francesco, J., Johnstone, D., et al. 2016a, ApJ, 817, 167

Kirk, H., Johnstone, D., Di Francesco, J., et al. 2016b, ApJ, 821, 98

Kiss, C., Ábrahám, P., Klaas, U., Juvela, M., & Lemke, D. 2001, A&A, 379, 1161

Koch, E. W., & Rosolowsky, E. W. 2015, MNRAS, 452, 3435

Könyves, V., André, P., Men'shchikov, A., et al. 2010, A&A, 518, L106

Könyves, V., André, P., Men'shchikov, A., et al. 2015, A&A, 584, A91

Kramer, C., Stutzki, J., Rohrig, R., & Corneliussen, U. 1998, A&A, 329, 249

Kroupa, P. 2001, MNRAS, 322, 231

Kroupa, P. 2008, IAU Symp., 246, 13

Lada, C. J., Forbrich, J., Lombardi, M., & Alves, J. F. 2012, ApJ, 745, 190

Ladjelate, B., André, P., Könyves, V., et al. 2019, A&A, accepted

Lallement, R., Vergely, J.-L., Valette, B., et al. 2014, A&A, 561, A91

Lombardi, M. 2009, A&A, 493, 735

Markwardt, C. B. 2009, ASP Conf. Ser., 411, 251

Marsh, K. A., Griffin, M. J., Palmeirim, P., et al. 2014, MNRAS, 439, 3683

Marsh, K. A., Kirk, J. M., André, P., et al. 2016, MNRAS, 459, 342

Megeath, S. T., Gutermuth, R., Muzerolle, J., et al. 2012, AJ, 144, 192

Megeath, S. T., Gutermuth, R., Muzerolle, J., et al. 2016, AJ, 151, 5

Men'shchikov, A. 2013, A&A, 560, A63

Men'shchikov, A. 2017, A&A, 607, A64

Men'shchikov, A., André, P., Didelon, P., et al. 2012, A&A, 542, A81

Menten, K. M., Reid, M. J., Forbrich, J., & Brunthaler, A. 2007, A&A, 474, 515

Myers, P. C. 1983, ApJ, 270, 105

Nielbock, M., Launhardt, R., Steinacker, J., et al. 2012, A&A, 547, A11

Ochsendorf, B. B., Brown, A. G. A., Bally, J., & Tielens, A. G. G. M. 2015, ApJ, 808, 111

Oliver, S. J., Wang, L., Smith, A. J., et al. 2010, A&A, 518, L21

Oliver, S. J., Bock, J., Altieri, B., et al. 2012, MNRAS, 424, 1614

Onishi, T., Mizuno, A., Kawamura, A., Ogawa, H., & Fukui, Y. 1998, ApJ, 502, 296

Orkisz, J. H., Pety, J., Gerin, M., et al. 2017, A&A, 599, A99

Ostriker, J. 1964, ApJ, 140, 1056

Palmeirim, P., André, P., Kirk, J., et al. 2013, A&A, 550, A38

Parker, R. J. 2018, MNRAS, 476, 617

Parker, R. J., & Goodwin, S. P. 2015, MNRAS, 449, 3381

Pety, J., Guzmán, V. V., Orkisz, J. H., et al. 2017, A&A, 599, A98

Pezzuto, S., Benedettini, M., Di Francesco, J., et al. 2019, A&A, submitted

Pilbratt, G. L., Riedinger, J. R., Passvogel, T., et al. 2010, A&A, 518, L1

Poglitsch, A., Waelkens, C., Geis, N., et al. 2010, A&A, 518, L2

Polychroni, D., Schisano, E., Elia, D., et al. 2013, ApJ, 777, L33

Pon, A., Ochsendorf, B. B., Alves, J., et al. 2016, ApJ, 827, 42

Press, W. H., Teukolsky, S. A., Vetterling, W. T., & Flannery, B. P. 1992, Numerical recipes in FORTRAN. The art of scientific computing, 2nd edn., (Cambridge: CambridgeUniversity Press)

Rosolowsky, E. W., Pineda, J. E., Kauffmann, J., & Goodman, A. A. 2008, ApJ, 679, 1338

Roy, A., André, P., Palmeirim, P., et al. 2014, A&A, 562, A138

Schneider, N., Bontemps, S., Simon, R., et al. 2011, A&A, 529, A1

Schneider, N., André, P., Könyves, V., et al. 2013, ApJ, 766, L17

Shimajiri, Y., André, P., Braine, J., et al. 2017, A&A, 604, A74

Shimajiri, Y., André, P., Ntormousi, E., et al. 2019, A&A, 632, A83

Sousbie, T. 2011, MNRAS, 414, 350

Tafalla, M., Myers, P. C., Caselli, P., Walmsley, C. M., & Comito, C. 2002, ApJ, 569, 815

Ward-Duong, K., Patience, J., De Rosa, R. J., et al. 2015, MNRAS, 449, 2618

Ward-Thompson, D., André, P., Crutcher, R., et al. 2007, in Protostars and Planets V, eds. B. Reipurth et al. (Tucson: University of Arizona Press), 33

Zucker, C., Speagle, J. S., Schlafly, E. F., et al. 2019, ApJ, 879, 125

Appendix A: Catalog of dense cores identified with *Herschel* in the Orion B cloud complex

With our *Herschel* SPIRE and PACS parallel-mode imaging survey of the Orion B cloud complex, we identified a total of 1844 dense cores, including 1768 starless cores and 76 protostellar cores. The master catalog listing the observed properties of all of these *Herschel* cores is available in Table A.1. A template of this online catalog is provided below to illustrate its form and content.

The derived properties (physical radius, mass, SED dust temperature, peak column density at the resolution of the 500 μm data, average column density, peak volume density, and average density) are given in Table A.2 for each core. A portion of this online table is also provided below.

The end of the catalog of observed core properties also includes 26 additional tentative cores which are possible extragalactic contaminants (see Sect. 3.5.2). The derived properties of these objects are not provided in Table A.2.

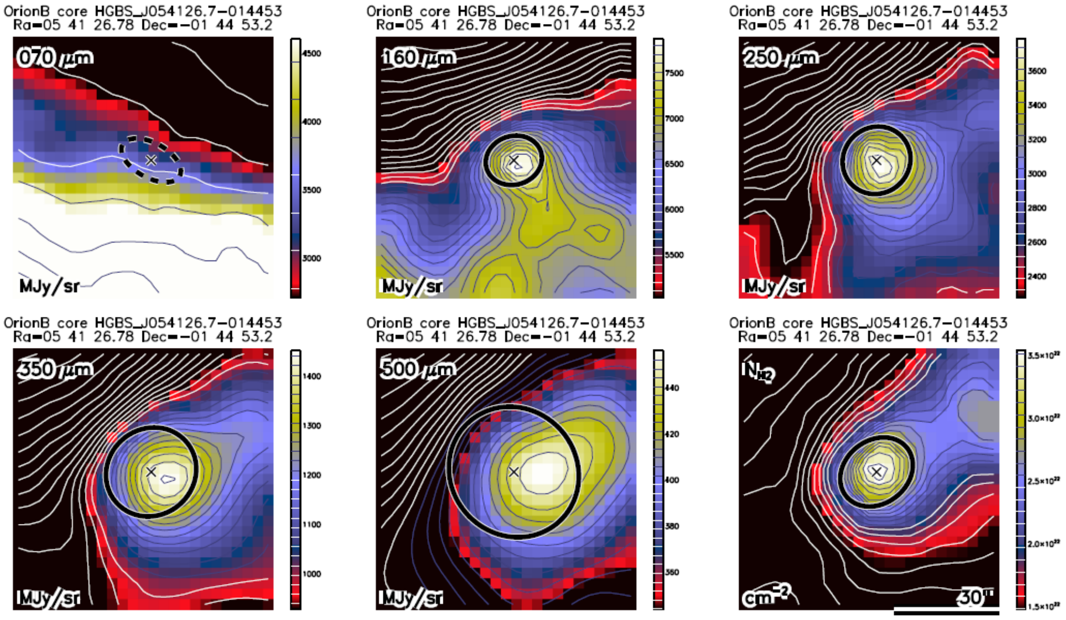

Fig. A.1. Example blow-up *Herschel* images at 70–160–250–350–500 μm and high-resolution column density map for a (bound) prestellar core. Ellipses represent the estimated major and minor FWHM sizes of the core at each wavelength; they are shown as solid or dashed curves depending on whether the core is significantly detected or not, respectively, at a particular wavelength. See Table A.2 for the physical radius of the core and other derived properties. An angular scale of 30″ (~0.058 pc at d = 400 pc) is shown at the bottom right. North is up, east is left. Similar image cutouts are provided online for all selected starless cores.

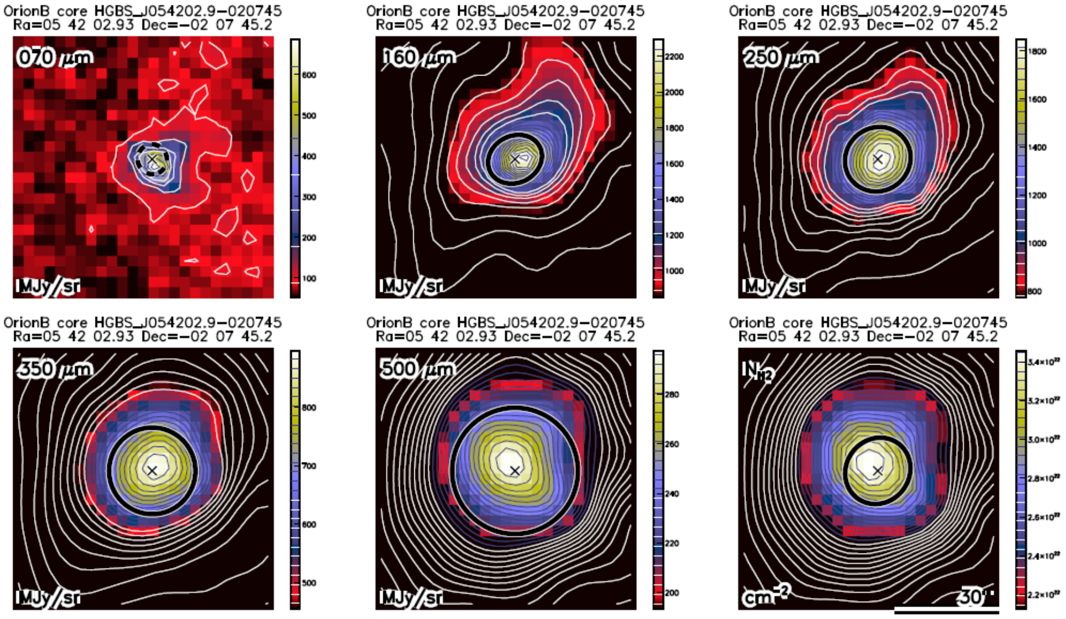

Fig. A.2. Same as Fig. A.1 for a protostellar core. See Table A.2 for its derived properties. Similar image cutouts are provided online for all selected protostellar cores.

Table A.1. Catalog of dense cores identified in HGBS maps of Orion B (template, full catalog only provided at the CDS).

rNO (1)	Core name HGBS_J* (2)	RA$_{2000}$ (h m s) (3)	Dec$_{2000}$ (° ′ ″) (4)	Sig$_{070}$ (5)	$S^{\rm peak}_{070}$ (Jy beam^{-1}) (6)	± (7)	$S^{\rm peak}_{070}/S_{\rm bg}$ (8)	$S^{\rm conv,500}_{070}$ (Jy beam^{-1}$_{500}$) (9)	$S^{\rm tot}_{070}$ (Jy) (10)	± (11)	$FWHM^{(a)}_{070}$ (″) (12)	$FWHM^{(b)}_{070}$ (″) (13)	PA$_{070}$ (°) (14)
…													
204	054126.7-014453	05:41:26.78	−01:44:53.2	0.0	−8.09e-01	8.1e-01	−0.00	−8.34e-02	1.03e+00	1.8e+00	−1	−1	−1
…													
428	054202.9-020745	05:42:02.93	−02:07:45.2	68.0	1.13e+00	1.9e-02	5.78	1.26e+00	1.76e+00	4.7e-02	9	8	24
…													
682	054316.0-025859	05:43:16.09	−02:58:59.0	0.0	8.37e-03	1.5e-02	0.10	9.79e-02	2.31e-01	3.5e-02	42	40	86
…													

Sig$_{160}$ (15)	$S^{\rm peak}_{160}$ (Jy/beam) (16)	± (17)	$S^{\rm peak}_{160}/S_{\rm bg}$ (18)	$S^{\rm conv,500}_{160}$ (Jy beam^{-1}$_{500}$) (19)	$S^{\rm tot}_{160}$ (Jy) (20)	± (21)	$FWHM^{\rm a}_{160}$ (″) (22)	$FWHM^{\rm b}_{160}$ (″) (23)	PA$_{160}$ (°) (24)	Sig$_{250}$ (25)	$S^{\rm peak}_{250}$ (Jy beam^{-1}) (26)	± (27)	$S^{\rm peak}_{250}/S_{\rm bg}$ (28)	$S^{\rm conv,500}_{250}$ (Jy beam^{-1}$_{500}$) (29)	$S^{\rm tot}_{250}$ (Jy) (30)	± (31)	$FWHM_{250}$$^{(a)}$ (″) (32)	$FWHM_{250}$$^{(b)}$ (″) (33)	PA$_{250}$ (°) (34)
…																			
279.3	9.10e+00	2.0e+00	0.35	1.21e+01	1.42e+01	3.2e+00	16	14	106	376.9	1.69e+01	2.0e+00	0.76	1.80e+01	2.33e+01	2.1e+00	20	19	130
…																			
228.6	8.30e+00	2.9e-01	1.93	1.04e+01	1.32e+01	4.2e-01	16	14	116	366.2	1.49e+01	5.0e-01	2.24	1.49e+01	1.94e+01	5.0e-01	19	18	125
…																			
6.8	1.65e-01	4.1e-02	0.15	6.11e-01	7.33e-01	9.2e-02	34	30	92	9.1	2.88e-01	4.0e-02	0.23	4.38e-01	6.63e-01	5.7e-02	28	24	−37
…																			

Sig$_{350}$ (35)	$S^{\rm peak}_{350}$ (Jy beam^{-1}) (36)	± (37)	$S^{\rm peak}_{350}/S_{\rm bg}$ (38)	$S^{\rm conv,500}_{350}$ (Jy beam^{-1}$_{500}$) (39)	$S^{\rm tot}_{350}$ (Jy) (40)	± (41)	$FWHM_{350}$$^{(a)}$ (″) (42)	$FWHM_{350}$$^{(b)}$ (″) (43)	PA$_{350}$ (°) (44)	Sig$_{500}$ (45)	$S^{\rm peak}_{500}$ (Jy beam^{-1}) (46)	± (47)	$S^{\rm peak}_{500}/S_{\rm bg}$ (48)	$S^{\rm tot}_{500}$ (Jy) (49)	± (50)	$FWHM_{500}$$^{(a)}$ (″) (51)	$FWHM_{500}$$^{(b)}$ (″) (52)	PA$_{500}$ (°) (53)
…																		
295.3	1.41e+01	1.9e+00	0.99	1.45e+01	1.77e+01	1.9e+00	27	25	127	196.8	9.92e+00	1.3e+00	1.25	1.26e+01	1.3e+00	39	36	45
…																		
362.8	1.31e+01	3.5e-01	2.34	1.30e+01	1.48e+01	3.5e-01	25	25	82	249.7	8.80e+00	1.7e-01	2.55	9.19e+00	1.7e-01	36	36	50
…																		
7.8	2.32e-01	5.0e-02	0.20	2.55e-01	3.28e-01	5.3e-02	31	25	1	0.0	1.52e-01	6.8e-02	0.13	1.22e-01	6.8e-02	36	36	4
…																		

Sig$_{N_{\rm H_2}}$ (54)	$N^{\rm peak}_{\rm H_2}$ (10^{21} cm^{-2}) (55)	$N^{\rm peak}_{\rm H_2}/N_{\rm bg}$ (56)	$N^{\rm conv,500}_{\rm H_2}$ (10^{21} cm^{-2}) (57)	$N^{\rm bg}_{\rm H_2}$ (10^{21} cm^{-2}) (58)	$FWHM_{N_{\rm H_2}}$$^{(a)}$ (″) (59)	$FWHM_{N_{\rm H_2}}$$^{(b)}$ (″) (60)	PA$_{N_{\rm H_2}}$ (°) (61)	N$_{\rm SED}$ (62)	Core type (63)	*Spitzer* (64)	SIMBAD (65)	Comments (66)
…												
313.6	18.0	1.25	5.2	14.4	22	18	127	4	2	0	[KDJ2016] J054126.7-014451	
…												
943.9	49.2	3.58	13.1	13.7	20	18	−40	4	3	1	[KDJ2016] J054202.7-020745, [MSJ2009] L1630MIR-94	
…												
9.1	0.5	0.24	0.2	1.9	31	18	24	3	1	0		
…												

Notes. Catalog entries are as follows: (1) core running number; (2) core name = HGBS_J prefix directly followed by a tag created from the J2000 sexagesimal coordinates; (3) and (4): right ascension and declination of core center; (5), (15), (25), (35), and (45): detection significance from monochromatic single scales, in the 70, 160, 250, 350, and 500 μm maps, respectively. (NB: the detection significance has the special value of 0.0 when the core is not visible in clean single scales); (6) ± (7), (16) ± (17) (26) ± (27) (36) ± (37) (46) ± (47): peak flux density and its error in Jy beam^{-1} as estimated by `getsources`; (8), (18), (28), (38), (48): contrast over the local background, defined as the ratio of the background-subtracted peak intensity to the local background intensity ($S^{\rm peak}_{\lambda}/S_{\rm bg}$); (9), (19), (29), (39): peak flux density measured after smoothing to a 36.3″ beam; (10) ± (11), (20) ± (21), (30) ± (31), (40) ± (41), (49) ± (50): integrated flux density and its error in Jy as estimated by `getsources`; (12)–(13), (22)–(23), (32)–(33), (42)–(43), (51)–(52): major and minor FWHM diameters of the core (in arcsec), respectively, as estimated by `getsources`. (NB: the special value of −1 means that no size measurement was possible); (14), (24), (34), (44), (53): position angle of the core major axis, measured east of north, in degrees; (54) detection significance in the high-resolution column density image; (55) peak H_2 column density in units of 10^{21} cm^{-2} as estimated by `getsources` in the high-resolution column density image; (56) column density contrast over the local background, as estimated by `getsources` in the high-resolution column density image; (57) peak column density measured in a 36.3″ beam; (58) local background H_2 column density as estimated by `getsources` in the high-resolution column density image; (59)–(60)–(61): major and minor FWHM diameters of the core, and position angle of the major axis, respectively, as measured in the high-resolution column density image; (62) number of *Herschel* bands in which the core is significant (Sig$_\lambda > 5$) and has a positive flux density, excluding the column density plane; (63) core type: 1-starless, 2-prestellar, 3-protostellar, or 0-tentative core. The latter is a likely extragalactic source; (64) 1 if a *Spitzer*-identified YSO (Megeath et al. 2012) is found within 6″ of the *Herschel* peak position, 0 otherwise (see text for details); (65) SIMBAD counterparts, if any, up to 6″ from the *Herschel* peak position; (66) comments: "N region".

Table A.2. Derived properties of dense cores identified in HGBS maps of Orion B (template, full table only provided at the CDS).

rNO	Core name	RA_{2000}	Dec_{2000}	R_{core}		M_{core}		T_{dust}		$N_{H_2}^{peak}$	$N_{H_2}^{ave}$		$n_{H_2}^{peak}$	$n_{H_2}^{ave}$		α_{BE}	Core type	Comments
	HGBS_J*	(h m s)	(° ′ ″)	(pc)		($M_\odot$)		(K)		(10^{21} cm^{-2})	(10^{21} cm^{-2})		(10^4 cm^{-3})	(10^4 cm^{-3})				
(1)	(2)	(3)	(4)	(5)	(6)	(7) ±	(8)	(9) ±	(10)	(11)	(12)	(13)	(14)	(15)	(16)	(17)	(18)	(19)
…																		
204	054126.7-014453	05:41:26.78	–01:44:53.2	2.1e-02	3.9e-02	8.80	2.07	11.1	0.6	59.0	68.2	233.9	24.8	38.2	242.5	0.0	2	
…																		
428	054202.9-020745	05:42:02.93	–02:07:45.2	1.8e-02	3.7e-02	6.17	1.17	11.5	0.5	56.9	54.4	235.6	24.3	32.5	292.7	0.1	3	
…																		
682	054316.0-025859	05:43:16.09	–02:58:59.0	2.9e-02	4.6e-02	0.05	0.02	15.7	1.7	0.2	0.3	0.7	0.1	0.1	0.5	11.4	1	
…																		

Notes. Table entries are as follows: (1) core running number; (2) core name = HGBS_J prefix directly followed by a tag created from the J2000 sexagesimal coordinates; (3) and (4): right ascension and declination of core center; (5) and (6): geometrical average between the major and minor FWHM sizes of the core (in pc), as measured in the high-resolution column density map after deconvolution from the 18.2″ HPBW resolution of the map and before deconvolution, respectively. (NB: both values provide estimates of the object's outer radius when the core can be approximately described by a Gaussian distribution, as is the case for a critical Bonnor-Ebert spheroid); (7) estimated core mass ($M_\odot$) assuming the dust opacity law advocated by Roy et al. (2014); (9) SED dust temperature (K); (8) and (10) statistical errors on the mass and temperature, respectively, including calibration uncertainties, but excluding dust opacity uncertainties; (11) peak H_2 column density, at the resolution of the 500 μm data, derived from a graybody SED fit to the core peak flux densities measured in a common 36.3″ beam at all wavelengths; (12) average column density, calculated as $N_{H_2}^{ave} = \frac{M_{core}}{\pi R_{core}^2} \frac{1}{\mu m_H}$, where M_{core} is the estimated core mass (col. 7), R_{core} the estimated core radius prior to deconvolution (col. 6), and $\mu = 2.8$; (13) average column density calculated in the same way as for col. 12 but using the deconvolved core radius (col. 5); (14) beam-averaged peak volume density at the resolution of the 500 μm data, derived from the peak column density (col. 11) assuming a Gaussian spherical distribution: $n_{H_2}^{peak} = \sqrt{\frac{4\ln 2}{\pi}} \frac{N_{H_2}^{peak}}{FWHM_{500}}$; (15) average volume density, calculated as $n_{H_2}^{ave} = \frac{M_{core}}{4/3\pi R_{core}^3} \frac{1}{\mu m_H}$, using the estimated core radius prior to deconvolution; (16) average volume density, calculated in the same way as for col. 15 but using the deconvolved core radius (col. 5); (17) bonnor-Ebert mass ratio: $\alpha_{BE} = M_{BE,crit}/M_{obs}$ (see text for details); (18) core type: 1-starless, 2-prestellar, 3-protostellar, or 0-tentative core. The latter is a likely extragalactic source (see comments); (19) comments: "no SED fit", "tentative bound", "N region".

Appendix B: Automated post-selection of reliable core candidates

The `getsources` source extraction algorithm (Men'shchikov et al. 2012), which analyzes fine spatial decompositions of the original images across a wide range of scales and at all observed wavebands, is a powerful technique to extract most candidate dense cores in spatially-varying backgrounds. At the same time, however, this technique tends to extract irregularities in the emission maps used for detection which must be discarded by the user at the post-selection stage, that is after the initial selection criteria described in Sect. 3.5.1 have been automatically applied.

The criteria of Sect. 3.5.1 are applied to the raw output catalog from `getsources`. At this stage, the properties of candidate cores are derived directly from `getsources` measurements without going back to the observed maps themselves. After the initial selection steps, there may still be a significant number of spurious sources in the selected core list which do not correspond to real emission peaks or do not appear like genuine cores in the maps. These spurious sources can only be eliminated by revisiting their locations in the *Herschel* maps, which is done here with a separate automated script. This "post-selection" script is run on the same input observed maps with 3″ pixels as used for the `getsources` extractions.

The automatic post-selection script, written in IDL, works without any free parameter. It performs further source selection and elimination according to the following steps:

1. The script prepares a close-up view of each core from the input source list at the standard HGBS wavelengths (70, 160, 250, 350, 500 μm), and in the high-resolution column density plane (see Figs. A.1, and A.2 for examples). Another example of a core at 500 μm is provided in Fig. B.1. The input source list of the post-selection stage is the output of the core selection procedure detailed in Sect. 3.5.1.

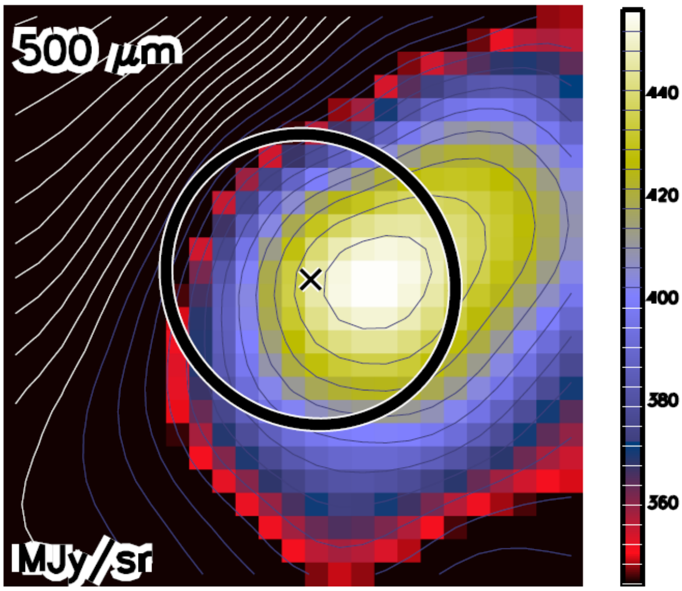

Fig. B.1. Close-up view of a post-selected prestellar core at 500 μm (shown in Fig. A.1) illustrating the post-selection procedure. At each wavelength, the map colorscale is optimized for the immediate neighborhood of the core; the lowest and highest map values in the considered box are blanked by black and white colors, respectively. The source center position is marked by a cross, and the FWHM ellipse automatically derived by `getsources` is plotted.

2. Annular masks are created inside and outside of the FWHM ellipse of a given source at each wavelength, which are expanded (or shrunk) versions of the FWHM elliptical footprint, scaling with radius, not with area. The division and numbering

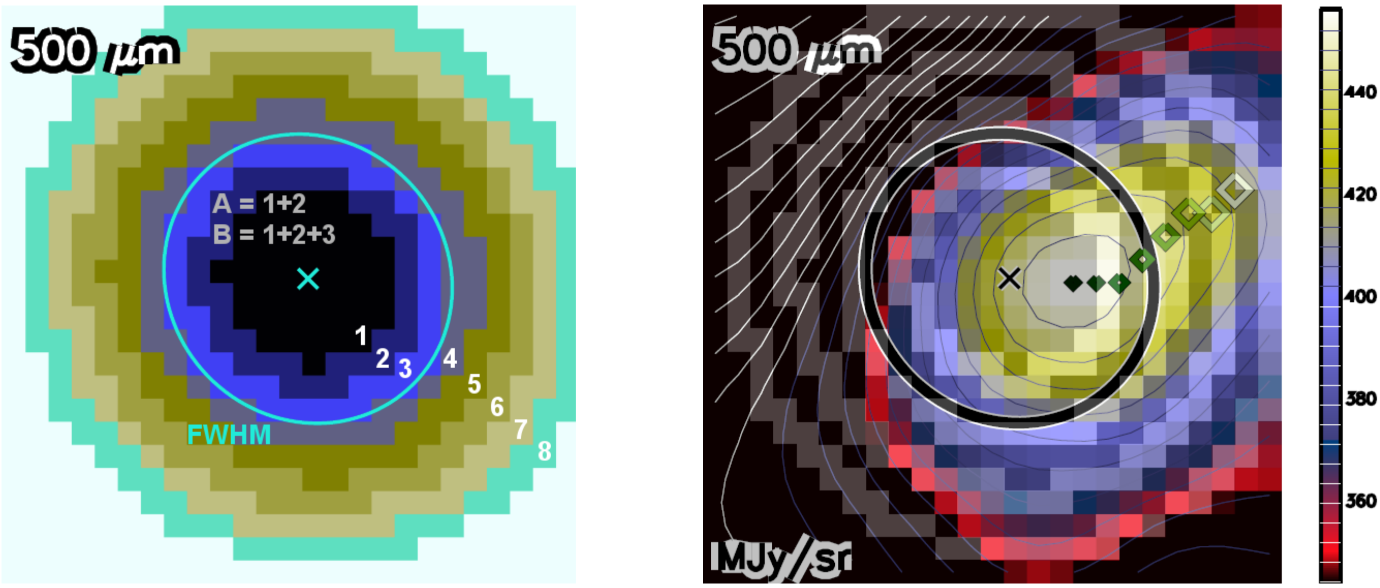

Fig. B.2. *Left*: examples of annular masks created inside and outside of the FWHM ellipse of each core at each wavelength. The example mask image shown here is at 500 μm and belongs to the prestellar core of Fig. B.1. Inside out, the division of the masks along the core radius is the following, considering the FWHM ellipse as 100%: region 1: <60% interior of the FWHM radius, region 2: 60–80%, 3: 80–100%, 4: 100–120%, 5: 120–140%, 6: 140–160%, 7: 160–180%, 8: 180–200%. Region A: <80% (regions 1+2), B: <100% (1+2+3). *Right*: the first maximum (i.e., the highest intensity pixel) in each mask is shown by a green-shaded diamond in the example image. The panel size, marked source center, and FWHM sizes are the same for each pair of mask image and observed image.

of these masks are illustrated in the left panel of Fig. B.2. We split the immediate neighborhood of each candidate core into the following masks, labeled by their linear sizes measured in units of the FWHM size (taken to be 100%). Region (1): elliptical area corresponding to a shrunk version of the FWHM footprint, within its 60% linear size; (2): region between the 60% and the 80% ellipse; (3): 80–100% mask; (4): 100–120% mask, (5): 120–140% mask; (6): 140–160% mask; (7): 160–180% mask; (8): 180–200% mask. Region A: elliptical area enclosed within the 80% ellipse (1 + 2); region B: area enclosed within the FWHM elliptical contour (i.e., <100% mask = 1 + 2 + 3).

3. In the next step, maxima are found in the observed images (at 160–250–350–500 μm, and at N_{H_2}) under the corresponding rings of masks (see right panel of Fig. B.2). The panel size, marked source center and FWHM sizes are the same for a pair of observed image and mask image at each wavelength. The location of the maximum value (i.e., the highest intensity pixel) in each consecutive annular mask map sections under the masks are is marked by a green-shaded symbol whose size increases with radius from nominal source center. At the same time, the script also locates the second and third intensity maximum points within each annular mask (not shown in Fig. B.2).

4. At this stage, when a core is post-selected at a certain observed wavelength, its *counter flag* (cntCoreλ) at that wavelength is assigned a value of 1, that is, cntCoreλ = 1. The default 0 value of cntCoreλ flips to 1 if:

I. the first maximum intensity values under the consecutive masks are decreasing outward from core center,

OR

II. the maximum intensity inside the FWHM area (region B) is higher than in the next mask outward (region 4),

OR

III. at least two of the secondary maxima in regions 1, 2, and 3 are larger than the first maximum in region 4,

OR

IV. the value of the third maximum in region 1 is larger than the first maxima in regions 2 and 3.

AND

V. the aspect ratio of the core ellipse is ≤3.

More precisely, at a certain wavelength, a candidate core is post-selected (kept) if at least one of the criteria from [I.] to [IV.] is satisfied, and if criterion [V.] is fulfilled at the same time.

5. The script then loops over the list of candidate cores to be post-selected, and analyzes each wavelength in turn. The final post-selection of a core is granted if cntCoreλ = 1 in at least three bands among the 160–250–350–500 μm images plus the high-resolution column density map.

In the case of Orion B, the fraction of discarded sources after applying the above procedure was ~30% of the input source list.

Our primary intention was to automate the post-selection checks of cores directly from the information contained in the observed *Herschel* maps, mimicking what a human eye would do. This script greatly facilitates the post-selection evaluation, but a final visual inspection is still recommended. As it was primarily designed for resolved dense cores, this procedure is not optimal for point-like sources or protostars.

Appendix C: Completeness of HGBS prestellar core extractions in Orion B

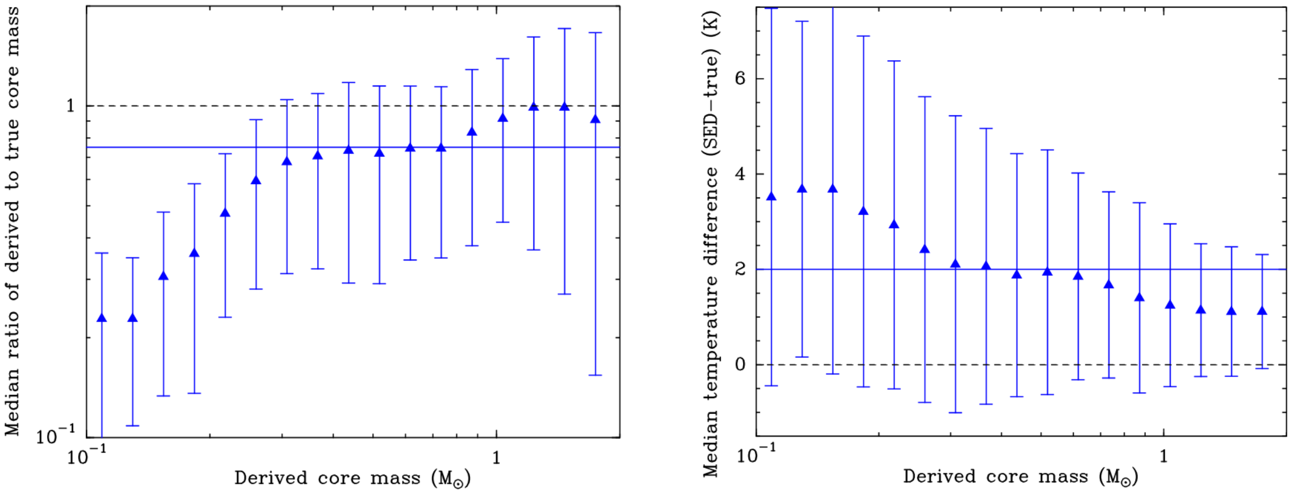

Fig. C.1. *Left*: ratio of measured to true core mass as function of measured core mass for the simulated core extractions. The error bars are $\pm 1\sigma$ where σ is the standard deviation of the mass ratio in each mass bin. The median mass ratio is ~0.75 for observed core masses between ~0.3 $M_\odot$ and ~0.8 $M_\odot$ (as indicated by the horizontal blue line). The horizontal dashed line indicates a mass ratio of 1, as expected for perfect core mass estimates. *Right*: difference between measured SED temperature and true mass-averaged dust temperature as function of measured core mass for the simulated core extractions. The error bars are $\pm 1\sigma$ where σ is the standard deviation of the temperature difference in each mass bin. The median temperature difference is approximately +2 K between ~0.3 $M_\odot$ and ~0.8 $M_\odot$ (as marked by the horizontal blue line), close to the fiducial completeness limit. The horizontal dashed line indicates no temperature difference, as expected for perfect core temperature estimates.

To assess the completeness of the present HGBS census of prestellar cores in Orion B, we used both simulated data and the simple model described in Appendix B.2 of Könyves et al. (2015).

To simulate core extractions, we constructed clean maps of the background cloud emission at *Herschel* wavelengths (plus a column density map), by subtracting the compact sources identified with `getsources` from the observed images (see Sects. 3.4 and 3.5). We then injected model Bonnor-Ebert-like cores within the clean-background maps to produce synthetic *Herschel* and column density images of the region. We used a population of 711 model starless cores with the following piecewise power-law mass distribution: $\Delta N/\Delta \log M \propto M^{+1.35}$ from 0.1 $M_\odot$ to 0.4 $M_\odot$, $\Delta N/\Delta \log M \propto M^{0}$ from 0.4 $M_\odot$ to 0.9 $M_\odot$, and $\Delta N/\Delta \log M \propto M^{-1.35}$ from 0.9 $M_\odot$ to 20 $M_\odot$. The positions of the model cores in a mass versus size diagram similar to that shown in Fig. 7 were consistent with critical Bonnor-Ebert isothermal spheres at effective gas temperatures ~ 7–20 K. The far-infrared and submillimeter continuum emission from the synthetic Bonnor–Ebert cores at all *Herschel* wavelengths was simulated using an extensive grid of spherical dust radiative transfer models generated with the MODUST code (e.g., Bouwman et al. 2000; Bouwman 2001). Accordingly, each synthetic prestellar core had a realistic dust temperature profile with a significantly lower dust temperature in its central inner part, as observed in resolved starless cores (cf. Roy et al. 2014). The synthetic cores were randomly distributed within the portions of the observed field where $N_{\mathrm{H}_2}^{\mathrm{bg}} \geq 5 \times 10^{21}$ cm^{-2} (or $A_\mathrm{V} \gtrsim 5$), without any mass segregation. Compact source extraction and core selection and classification were subsequently performed with `getsources` in the same manner as for the real observations (see Sects. 3.4 and 3.5).

As stated in Sect. 3.8 and illustrated in Fig. 8, the results of these Monte–Carlo tests indicate that the present *Herschel* census of prestellar cores in Orion B is ~80% complete down to ~0.5 $M_\odot$ in true core mass.

The above Monte–Carlo simulations were used to estimate the accuracy of the derived parameters such as core mass, radius, and dust temperature by comparing the measured values after core extraction to the intrinsic values of the model cores. Figure C.1 (left) shows that the measured core masses typically underestimate the true core masses by ~25% on average, and Fig. C.1 (right) suggests that the derived SED temperatures typically overestimate the true mass-averaged dust temperatures of the cores by typically ~2 K, around the fiducial completeness limit of ~0.4 $M_\odot$ in observed mass. A similar comparison for the core sizes (Fig. C.2) indicates that the measured sizes (prior to deconvolution) are within ~5% of the true core sizes on average. Since the core masses are underestimated when the dust temperatures are overestimated, the slight bias of the derived masses (Fig. C.1 left) can be interpreted as a direct consequence of the temperature overestimation (Fig. C.1 right). The latter is because the dust temperature derived from SED fitting exceeds the mass-averaged dust temperature of starless cores owing to the presence of an internal dust temperature gradient rising outward (see, e.g., Roy et al. 2014). Accounting for the ~25% effect on the derived masses, we estimate that the ~80% completeness limit at ~0.5 $M_\odot$ in *true* core mass is located at ~0.4 $M_\odot$ in *observed* core mass.

Figure C.3 confirms that the prestellar CMF can be reliably determined down to a fiducial completeness limit of ~0.4 $M_\odot$ in observed mass. A Kolmogorov–Smirnov (K–S) test shows that the derived CMF (blue histograms in Fig. C.3) is statistically indistinguishable (at the ~90% confidence level) from the input mass function (red curve in Fig. C.3) above 0.4 $M_\odot$. We also point out that the mass function of extracted *candidate* prestellar cores (light blue histogram in Fig. C.3) starts to deviate from the mass function of *robust* prestellar cores (dark blue histogram) below ~0.4 $M_\odot$, implying that the selection of bona fide self-gravitating starless cores becomes quite uncertain below the fiducial completeness limit. Indeed, the sample of *candidate* prestellar cores includes a significant number of

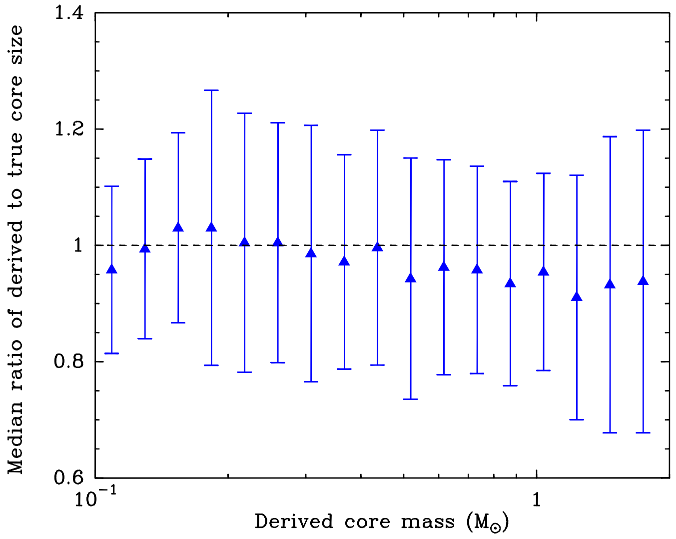

Fig. C.2. Ratio of measured to (convolved) intrinsic core size as function of measured core mass for simulated core extractions. The error bars are ±1σ where σ is the standard deviation of the size ratio in each mass bin. The horizontal dashed line indicates a size ratio of 1, as expected for perfect core size estimates.

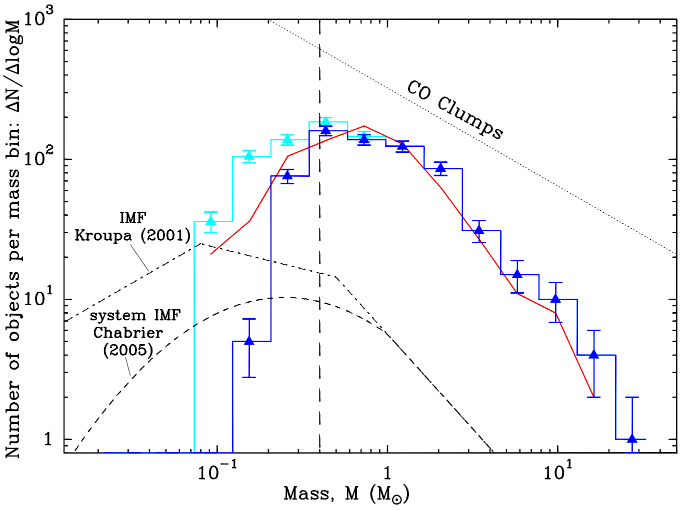

Fig. C.3. Synthetic prestellar core mass function (CMF) derived from simulated source extractions (blue histograms) compared to the input mass function of 711 model cores (red curve) constructed as described in the text. The light blue and dark blue histograms show the mass functions of the extracted *candidate* and *robust* prestellar cores, respectively. The estimated 80% completeness level of our *Herschel* census of prestellar cores in Orion B is indicated by the vertical dashed line at 0.4 $M_\odot$ (in observed core mass).

non-self-gravitating or spurious objects below this limit. Conversely, the sample of *robust* prestellar cores becomes severely incomplete.

As the rms level of background emission fluctuations (often referred to as "cirrus confusion noise") generally increases with column density (cf. Kiss et al. 2001 and Fig. B.4 in Könyves et al. 2015), the completeness level of our census of prestellar cores is background dependent and becomes worse in areas with higher background cloud emission. To estimate the variations of the completeness level in the observed field, we used the simple model of the core extraction process and completeness problem presented in Appendix B.2 of Könyves et al. (2015) for the Aquila cloud. This model, scaled to the distance of Orion B, allowed us to estimate individual completeness curves as a function of background column density, as shown in Fig. C.4. A global completeness curve (shown by the dashed blue curve in Fig. 8) was then computed as a weighted average of the individual completeness curves using the observed distribution of mass in the cloud as a function of background column density (cf. Fig. 4 here and Appendix B.2 of Könyves et al. 2015 for further details).

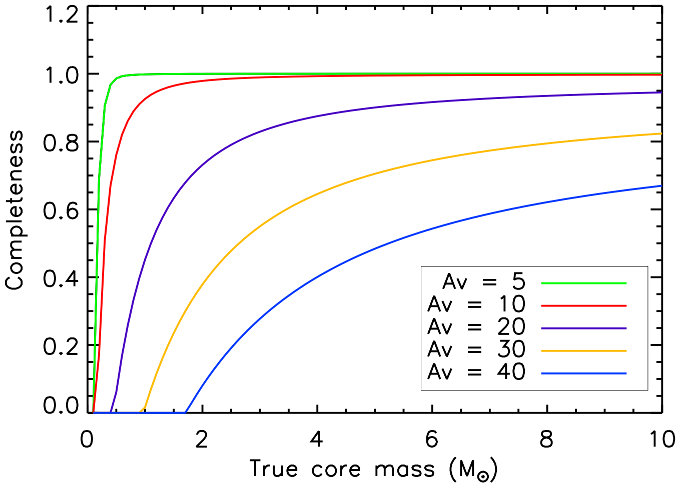

Fig. C.4. Model completeness curves of *Herschel* prestellar core extractions in Orion B for five values of background cloud column density expressed in units of visual extinction from $A_V^{bg} = 5$ to $A_V^{bg} = 40$.

Appendix D: Spatial clustering of prestellar cores in different mass regimes

D.1. Clustering of dense cores

The spatial clustering of dense cores can be defined and investigated with many methods (e.g., Kirk et al. 2016b; Gutermuth et al. 2009). Here, we used dendrograms (Rosolowsky et al. 2008) to define groups or clusters of cores. We utilized the IDL functions CLUSTER_TREE and DENDRO_PLOT separately for the *robust* prespellar core sample in the northern, middle, and southern tiles, separated by the declination lines at $\mathrm{Dec}_{2000} = 1°31'55''$, and $\mathrm{Dec}_{2000} = -0°28'38''$. Based on the column density distribution in the entire field, this seems to be a valid choice. A clear and simple example of a hierarchical clustering is shown in Fig. D.1 for the northern region L1622.

In this figure, the labeled individual cores are arranged in the bottom of the dendrogram. In the jargon they are referred to as leaves, marked by the lowest vertical lines, and they have no substructures. The horizontal lines connect leaves, then higher hierarchy levels, making branches. The point where a vertical line originates from a horizontal one is called a "node". Its height represents the distance (in parsec) between the left and right branches. The elements (i.e., cores) of these branches can also be called clusters.

In order to select clusters for our analysis, the dendrogram trees were inspected, and cores within 3 pc separation of each other in a branch were selected. We required a minimum number of 12 core elements. If a bigger cluster had significant sub-branches, we split it again into smaller clusters, typically at ~1.5 − 2 pc distances. Their properties can be studied separately, or together in larger clusters. This way, we found one

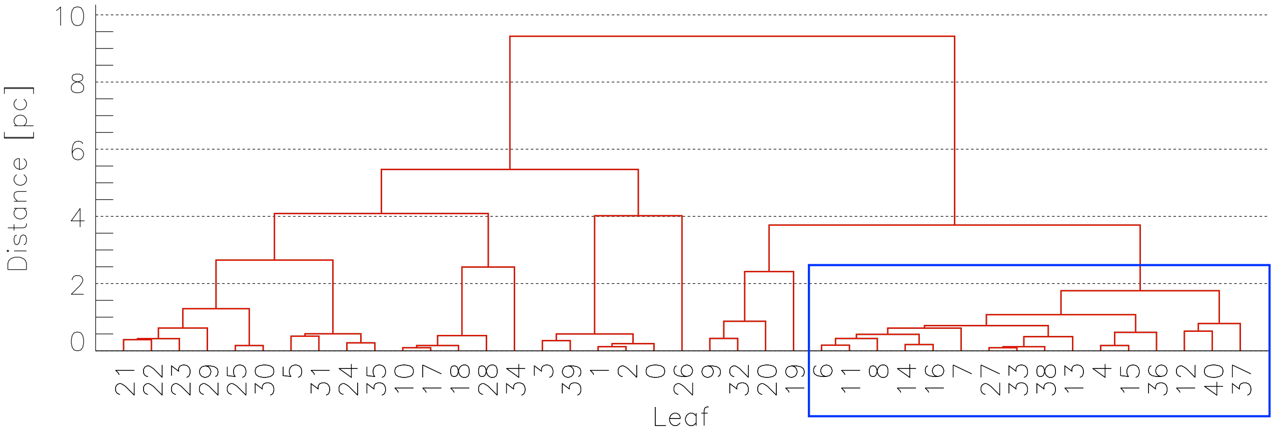

Fig. D.1. Dendrogram tree used for selecting cores in L1622. The leaves represent the list of cores in the northern part of Orion B (Dec$_{2000}$ > 1°31′55″). The 16 cluster members in this case were selected from leaves 6 to 37, marked by the blue rectangle. The red vertical connections projected on the Y axis show the distance between leaves and branches (see text for details).

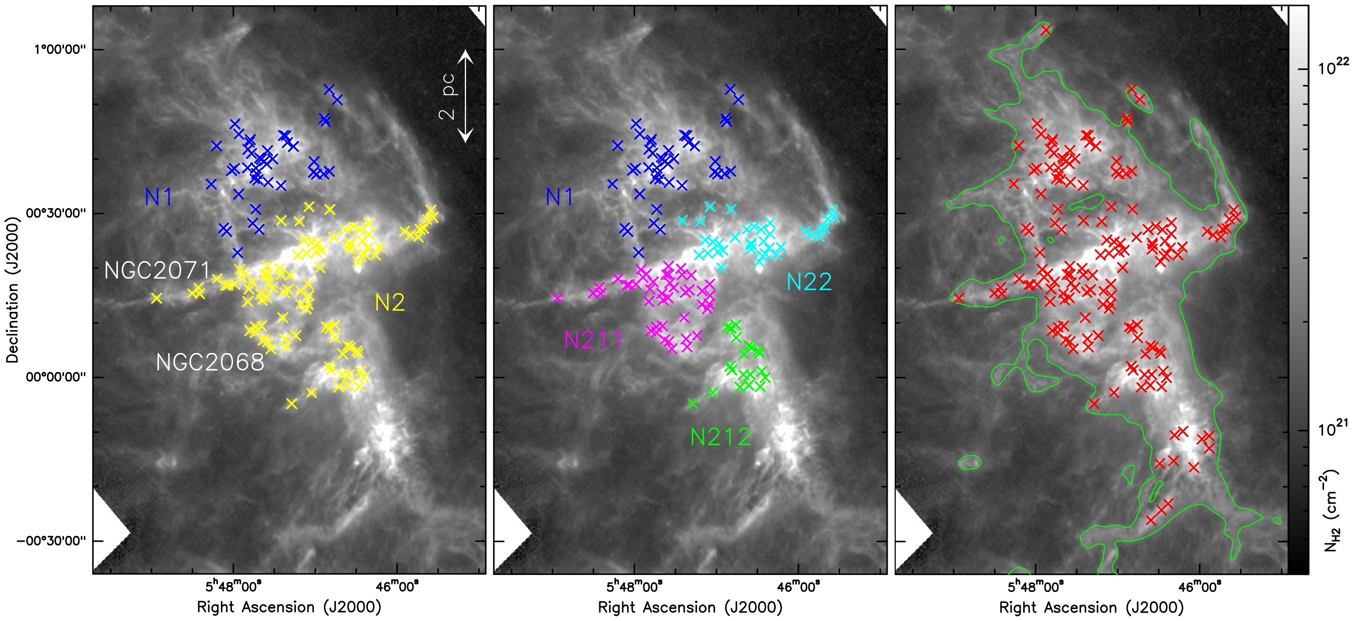

Fig. D.2. Clusterings of *robust* prestellar cores in NGC 2068 and 2071 of Orion B, defined mainly using dendrograms. The selected clusters are displayed in different colors, overplotted on the column density map of NGC 2068 and 2071. The *left panel* shows a bigger cluster (N2 in yellow), where cores were selected within 3 pc distances from one another in a branch of the dendrogram tree around NGC 2068 and 2071 (see text). A similar dendrogram tree is shown in Fig. D.1 for L1622. The *middle panel* displays subclusters of the N2 group. The cores within these smaller clusters are closer to each other than ~1.5 − 2 pc. In the *right image*, an arbitrary column density level of about 2 × 10^{21} cm^{-2} defines a group of cores in the region of NGC 2068 and 2071.

cluster containing 16 *robust* prestellar cores around L1622 in the north of Orion B (see Fig. D.1). The left and middle panels of Fig. D.2 (and Fig. D.3) display the various clusters of *robust* prestellar cores in the NGC 2068 and 2071 regions based on the above selection from their dendrogram trees. The number of core elements in these clusters are as follows: cluster N1: 43 cores, cluster N2: 100, N22: 36, N211: 44, N212: 20.

The CLUSTER_TREE function was run with the LINKAGE keyword (=2) which uses a weighted pairwise average. The distance between two leaves and clusters is defined as the average distance for all pairs of objects between each cluster, weighted by the number of objects in each cluster. We chose this method because it works well both for homogeneous clusters and for chain-like clusters. We indeed trace rather elongated, and more compact (sub)clusters as well.

Although these clustering properties stem only from the extracted core positions, the resulted clusters correlate very well with underlying column density features, including filaments, along which most of the cores are found. If we compare Fig. 9 (left panel) and Fig. D.2, we find eye-catching chains of cores along filaments. Using this idea, we also set an arbitrary column density level of about 2 × 10^{21} cm^{-2} to select another group of cores in the region of NGC 2068 and 2071 (right panel of Fig. D.2). With various clusters over the same region we can test if certain trends of core properties hold on different spatial scales.

D.2. Mass segregation of dense cores with the MST method

Figure 12 in Sect. 4.2 indicates that the most massive prestellar cores in our sample are spatially segregated in the highest

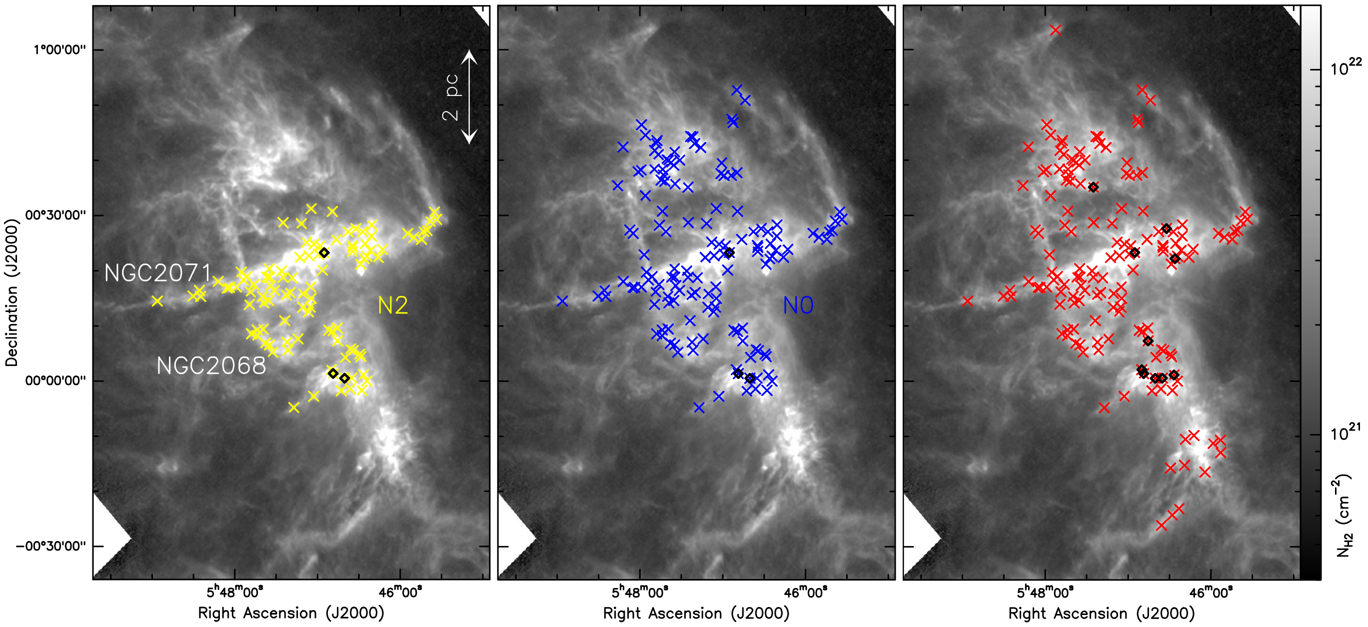

Fig. D.3. Alternative groupings of *robust* prestellar cores in NGC 2068 and 2071. The *left panel* shows the N2 cluster, the *middle panel* the N0 = N1 + N2 clusters (see left panel of Fig. D.2), and the *right panel* all cores lying above ~2 × 10^{21} cm^{-2} in this area (see right panel of Fig. D.2). Black open diamonds mark the 3 (*left and middle panels*) or 10 (*right panel*) most massive prestellar cores in these clusters.

column density portions of the Orion B complex. This mass segregation can also be quantified using the minimum spanning tree (MST) technique (e.g., Allison et al. 2009; Parker & Goodwin 2015). We applied this technique to the clusters of dense cores defined with the help of dendrograms in Appendix D.1. The MST method compares the minimum spanning tree of a given number N of the most massive cores with that of a randomly distributed population of cores. The observed and random MSTs are constructed from graphs where the shortest possible separations are calculated between cores, without allowing closed loops. If mass segregation is present, the MST length of the most massive cores in the sample should be significantly shorter than that of a random population of cores. The degree of mass segregation can be quantified via the mass segregation ratio, Λ_{MSR}, defined as the ratio of the average MST length for N randomly chosen cores to the MST length for the N most massive cores in the sample (Allison et al. 2009; Parker 2018). The Λ_{MSR} should significantly exceed 1 when mass segregation is present.

Figure D.4 shows a mass segregation ratio plot, in which MST calculations were applied to the N2 cluster of NGC 2068 and 2071 (see left panel of Fig. D.2). With a sliding window of three cores, the N2 cluster shows an explicit positive mass segregation ($\Lambda_{\mathrm{MSR}} > 6$), where the most massive cores in this region with $M > 10\,M_{\odot}$ are more concentrated spatially than cores with lower masses (left panel of Fig. D.3). However, comparing and contrasting the panels of Fig. D.3 with the summary table of mass segregation properties in various core clusters (Table D.1), it does not appear obvious that the three most massive cores in the N2 cluster are much more concentrated than the –same– three most massive cores in the N0 (=N1+N2) cluster (see middle panel of Fig. D.3). After carefully inspecting the values in Table D.1, the overall result in NGC 2068 and 2071 provides only marginal evidence for other than a random distribution of core masses, even though in one case the segregation of the most massive cores is strong (i.e., Fig. D.4). Further caveats and assumptions of the Λ_{MSR} method are discussed in detail in, for example, Parker (2018).

Finding some degree of mass segregation at the prestellar core stage in Orion B would lend support to the idea of primordial mass segregation in stellar protoclusters. Mass segregation at birth may be expected since protostellar sources embedded in denser filaments can accrete longer before feedback effects stop further gas inflow. This effect differs from the dynamical mass segregation quickly affecting evolved stars in revealed star clusters (e.g., Kroupa 2008).

Using published dense core samples from both the HGBS and ALMA (Atacama Large Millimeter Array) observations, Dib & Henning (2019) performed structure and mass segregation studies that they linked to the star formation activity of their set of clouds. They claim that the level of core mass segregation is positively correlated with the surface density of the star formation rate in the cloud. They attribute this correlation to a dependence on the physical conditions that have been imprinted by the large scale environment at the time these clouds started to form.

Based on dense cores in Orion B from JCMT's SCUBA-2 observations, Kirk et al. (2016b) and Parker (2018) analyzed the clustering and mass segregation properties by various methods. While Kirk et al. (2016b) found segregation of massive cores in NGC 2068 and 2071, and in NGC 2023 and 2024, according to Parker (2018), only a mild mass segregation is present in the NGC 2068 and 2071 regions. Our above findings seem to approach these latter results. However, we issue here a word of caution: the conclusions on mass segregation may depend somewhat on the chosen cluster and the exact method of analysis.

D.3. Core masses versus core surface density

As we have shown in Sect. 4.2, the presence of prestellar cores is strongly correlated with the local column density in the ambient cloud. This relationship is perhaps not surprising as dense cores require sufficient gas (at high column- and volume density) to form in the first place. In this appendix we present some initial results on the distributions of cores relative to each other (which will be investigated in more detail in a later paper).

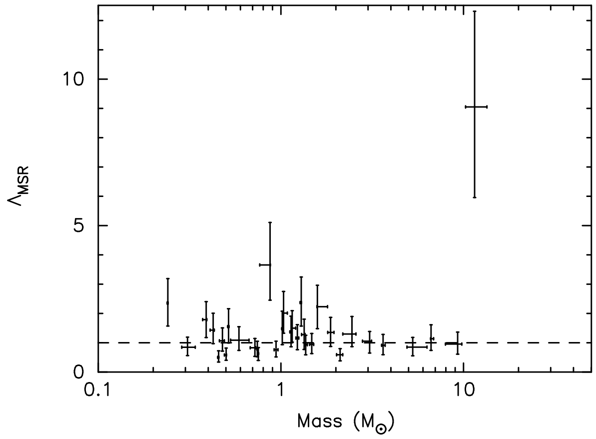

Fig. D.4. Mass segregation ratio, Λ_{MSR}, as function of core mass in the N2 cluster of NGC 2068 and 2071, including 100 *robust* prestellar cores (see left panel of Fig. D.2). The tool used to derive Λ_{MSR} is described in Allison et al. (2009). A sliding window of three cores ($N = 3$) was set in this case.

Table D.1. Mass segregation results with Λ_{MSR} method (based on Allison et al. 2009) in various core clusters of NGC 2068 and 2071.

	$N = 2$	$N = 3$	$N = 5$	$N = 10$
N11	0	0		
N1		0	0	
N2		4	2	2
N22		0	0	
N211		0	0	
N212	0	1	0	
N0 (N1+N2)		0	1	2
N22+N211		1	1	0
robust pre $>2 \times 10^{21}$ cm^{-2}		0	2	3
cand. pre $>2 \times 10^{21}$ cm^{-2}		0	2	3

Notes. This table summarizes results on mass segregation using various core samples that are listed in the left column (see Fig. D.2 and text for details). The assigned numbers in the table from 0 to 4 correspond to a range of *No* to *Strong* in properties of mass segregation. In a given cluster we analyzed the spatial distribution of cores against the $N = 2$, 3, 5, 10 highest mass cores in that cluster, provided that this was reasonable based on the size of the cluster (table cells are empty if not).

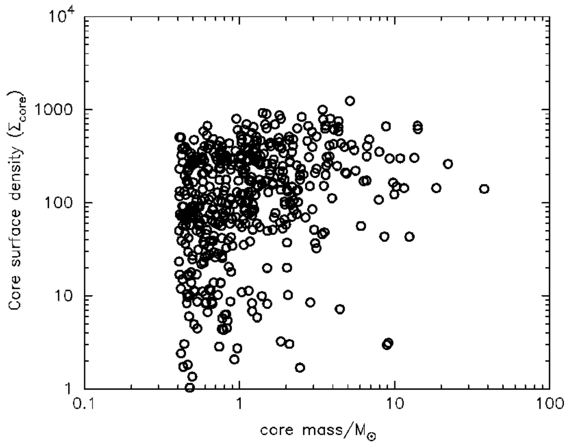

Fig. D.5. Distribution of core surface number densities (in angular area units) against core mass (in $M_\odot$). The sample of *robust* prestellar cores was used above 0.4 $M_\odot$.

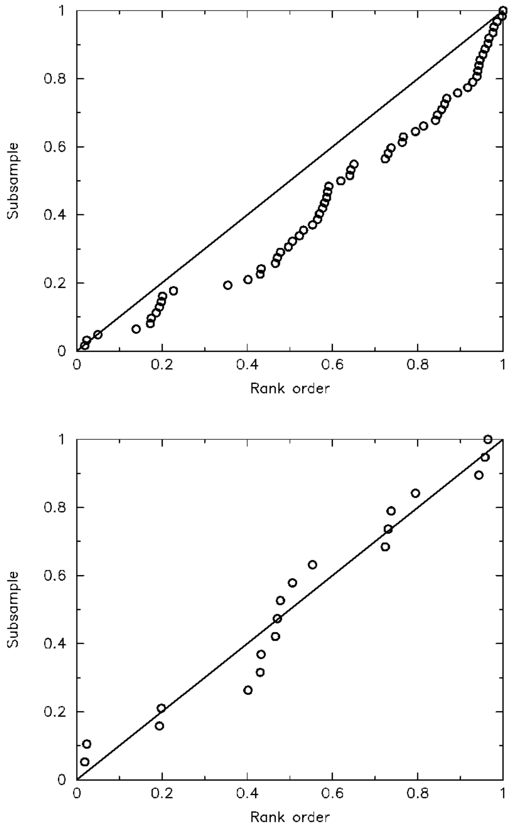

Fig. D.6. Cumulative distribution function of core positions (open circles) in ordered list of 423 core surface densities. *Top*: positions of 62 cores with masses $>3\,M_\odot$. *Bottom*: 19 most massive cores ($>7\,M_\odot$). See text for explanation.

We consider the sample of 423 *robust* prestellar cores, with masses $>0.4 M_\odot$ above the completeness limit (see Sect. 3.8). The core surface number density, $\Sigma_{\rm cores}$, is defined from the radius containing the 6 nearest neighbors, r_6, as $\Sigma_{\rm cores} = 6/r_6^2$ (cf. Casertano & Hut 1985). Very low values of $\Sigma_{\rm cores}$ indicate that cores are relatively isolated, very high values of $\Sigma_{\rm cores}$ that there are many cores close-by.

From the results of Sect. 4.2, we know that the most massive cores are in the areas with the highest background column density. An interesting related question to ask is whether the highest-mass cores are also found in regions of highest core surface density. In Fig. D.5, we show a plot of core surface number density (using arbitrary angular area units) against core mass. It is immediately obvious that there is no strong correlation between core mass and core surface density.

We can analyze Fig. D.5 more quantitatively using a Gini-like statistic (Gini 1912; Ward-Duong et al. 2015, see the latter for an astrophysical application). In an ordered list of cores by surface density we can quantify if a subset of cores (e.g., those with the highest masses) are consistent with being randomly distributed in the list (i.e., looking for a bias in what surface density those cores are found at).

As an example, the upper panel of Fig. D.6 shows the positions in an ordered list of all 423 core surface densities (the x-axis), and a cumulative distribution function (CDF) of the positions of the 62 cores with masses $>3 M_\odot$ (open circles). If the cores with masses $>3M_\odot$ were randomly distributed in the list then we would expect them to roughly follow the diagonal line (i.e., be equally likely to be anywhere in the list). The clear deviation from randomness can be quantified by calculating the area under the actual distribution and comparing it to a large ensemble of samples of 62 cores taken randomly from the list. If the distribution were random we would expect the area under the CDF to be 0.51 ± 0.03 (1σ error), while the actual area is 0.38. More usefully dividing the true by the expected values we have a quantity $\Sigma^+_{\rm cores} = 0.76 \pm 0.03$ (formally 5σ from random, although the distribution of random areas is not normally distributed in the tails). More qualitatively, this discrepancy is because cores $>3M_\odot$ are very unlikely to be at low core surface densities (only 25% of them are in the lowest 50% of core surface densities), and very likely to be at high core surface density (a third of them are in the top 20% of core surface densities). A strong correlation between core mass and local core surface density was also found based on the SCUBA-2 data in Orion B (Kirk et al. 2016b).

However, if we take only the 19 most massive *Herschel* cores $>7\,M_\odot$, as shown in the lower panel of Fig. D.6, we find that the most massive cores are completely consistent with being randomly distributed in core surface density with $\Sigma^+_{\rm cores} = 0.95 \pm 0.05$ (where unity is consistent with random). This is telling us that all cores with $>3M_\odot$ have a strong bias to be in regions of high core surface density, the trend is not following a simple higher-mass higher-core surface density relationship, and the very highest-mass cores could be "different" in some way and certainly show no signatures that could be easily interpreted as "mass segregation".

Appendix E: Additional figures

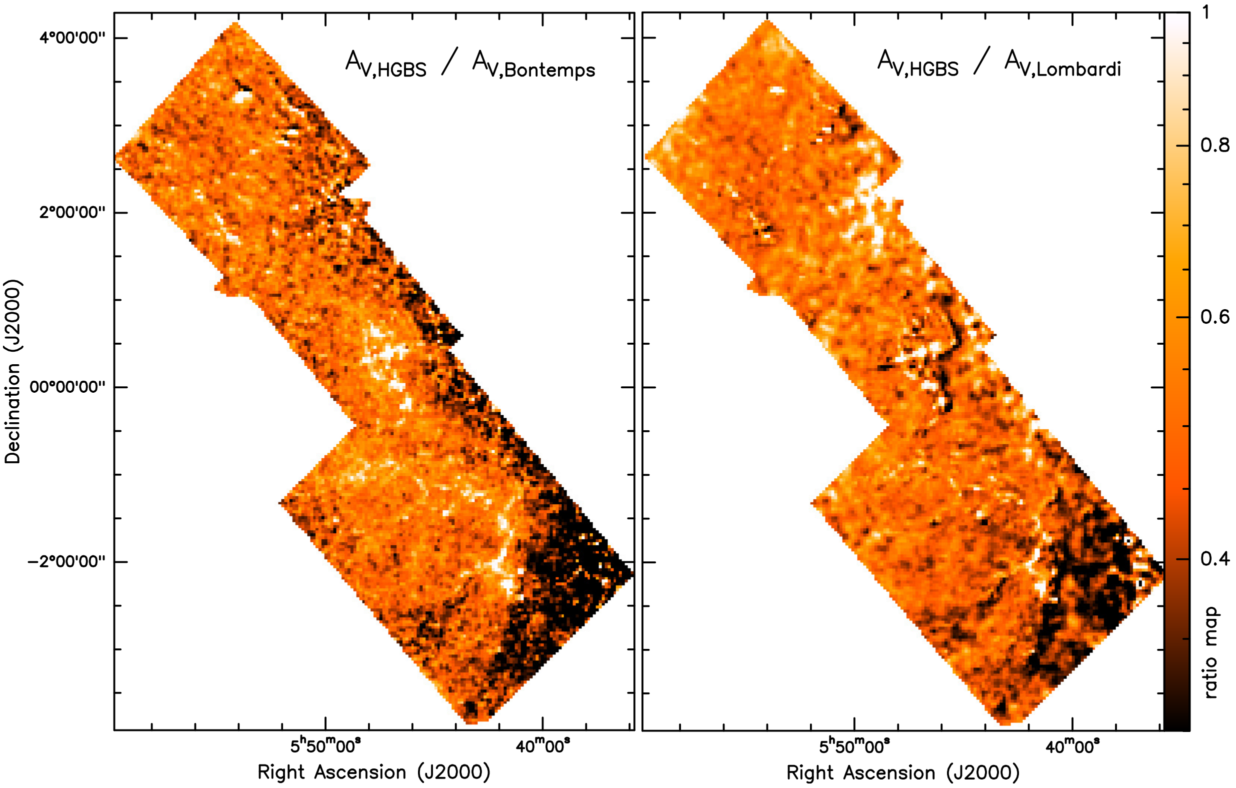

Fig. E.1. *Left*: map of the ratio of A_V-converted column density from HGBS data to visual extinction from Bontemps et al. *Right*: map of the ratio of A_V-converted column density from HGBS data to visual extinction from Lombardi et al. The median values of both ratio maps are ~0.5 (see Sect. 3.1 for details).

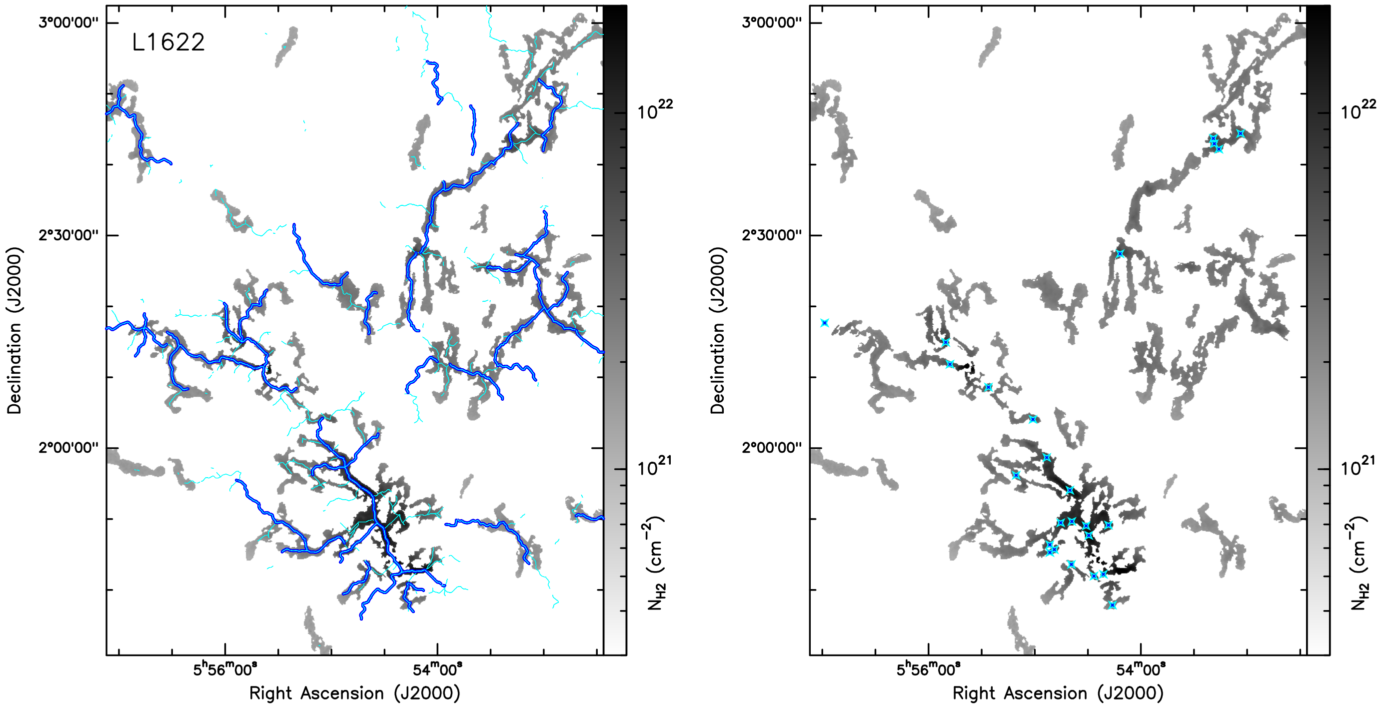

Fig. E.2. L1622 cloud and its surroundings. The gray background image shows the mask of filamentary network traced by `getfilaments` (Men'shchikov 2013). Within the `getfilaments` mask the color scale represents column density values in the column density map (Fig. 2 left). Angular scales up to 100″ are shown, which corresponds to ∼0.2 pc at $d = 400$ pc. *Left*: overplotted thicker blue skeletons mark the robust filament crests from the DisPerSE (Sousbie 2011) sample (see Sect. 3.2 for details). The latter sample together with the thin cyan crests make the DisPerSE raw sample of filaments. *Right*: overplotted blue crosses mark *robust* prestellar cores in the northern region.

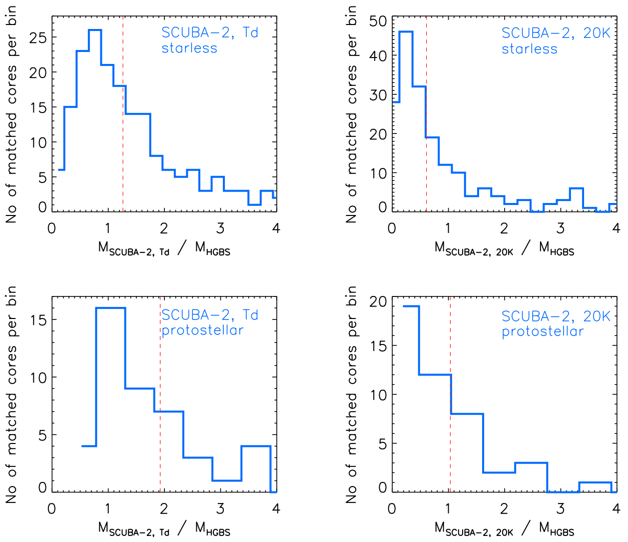

Fig. E.3. Ratios of SCUBA-2 to HGBS core mass estimates for matched starless and protostellar pairs within 6″. The SCUBA-2 core masses were re-derived assuming either 1) the dust temperatures estimated from *Herschel* SED fitting ($T_{\rm d}^{\rm SED}$), or 2) a uniform dust temperature of 20 K for all cores. In each panel, the median ratio is marked by a red dashed line (see details in Sect. 3.6).